

3D Imaging Reveals Changes in the Neurovascular Architecture of the Murine Calvarium with Aging

Allison L. Horenberg,^{1,2} Yunke Ren,^{1,2} Alexandra N. Rindone,^{1,2} Arvind P. Pathak,^{1,3-6}
Warren L. Grayson*^{1,2,6-8}

¹Department of Biomedical Engineering, Johns Hopkins University School of Medicine, Baltimore, MD, USA

²Translational Tissue Engineering Center, Johns Hopkins University School of Medicine, Baltimore, MD, USA

³Russell H. Morgan Department of Radiology and Radiological Sciences, the Johns Hopkins University School of Medicine, Baltimore, Maryland, USA

⁴Sidney Kimmel Comprehensive Cancer Center, the Johns Hopkins University School of Medicine, Baltimore, Maryland, USA

⁵Department of Electrical Engineering, Johns Hopkins University, Baltimore, Maryland, USA

⁶Institute for Nanobiotechnology, Johns Hopkins University, Baltimore, Maryland, USA

⁷Department of Materials Science and Engineering, Johns Hopkins University, Baltimore, MD, USA

⁸Department of Chemical and Biomolecular Engineering, Johns Hopkins University, Baltimore, MD, USA

*Corresponding author: wgrayson@jhmi.edu

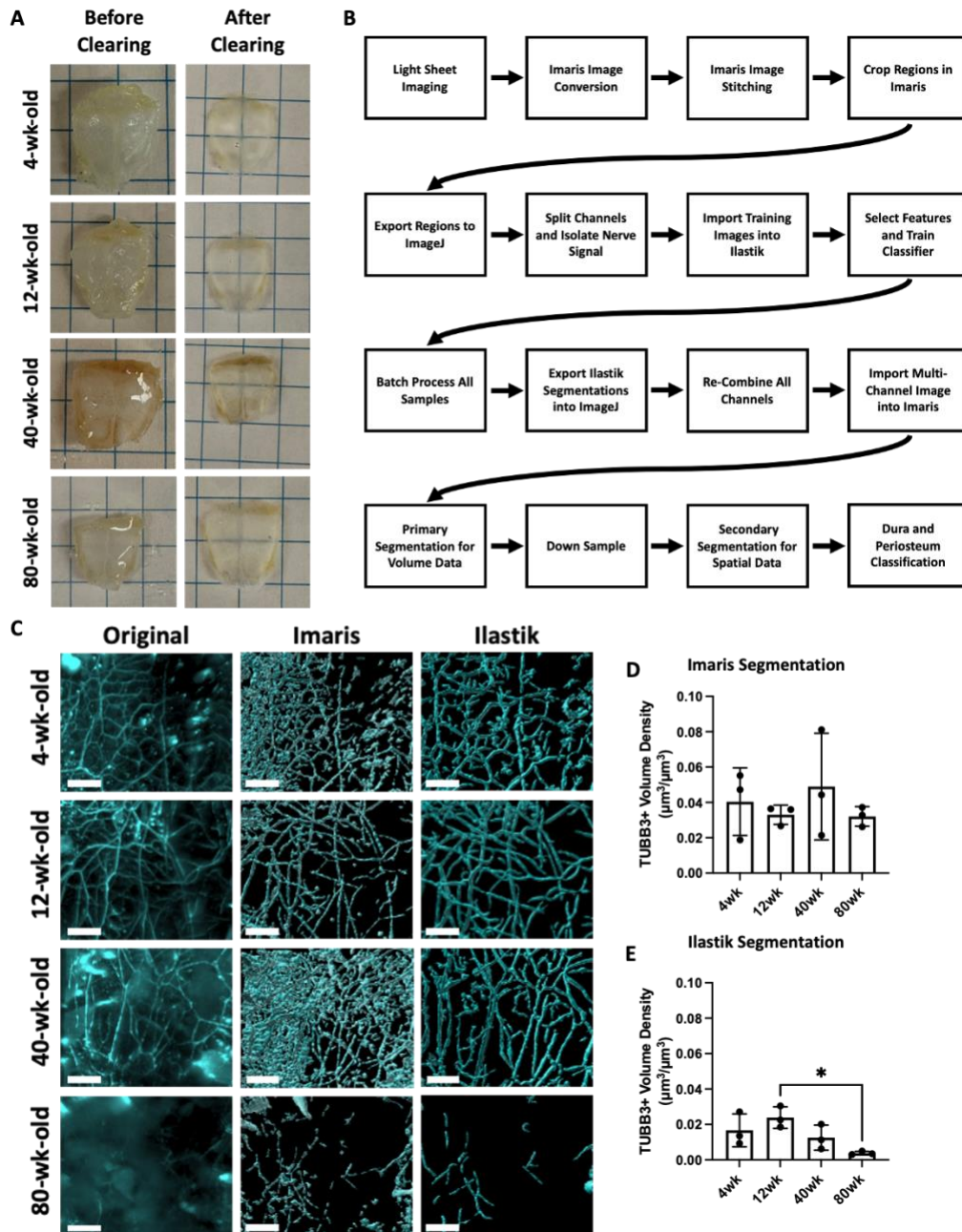
[400 N. Broadway](#)
[Smith 5023](#)
[Baltimore, MD, 21231](#)

ahorenb1@jhmi.edu

yren26@jhmi.edu

arindon1@jhmi.edu

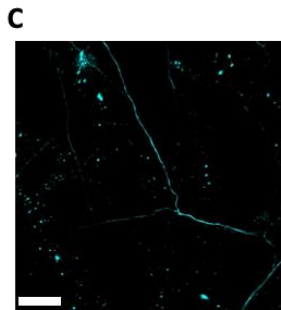
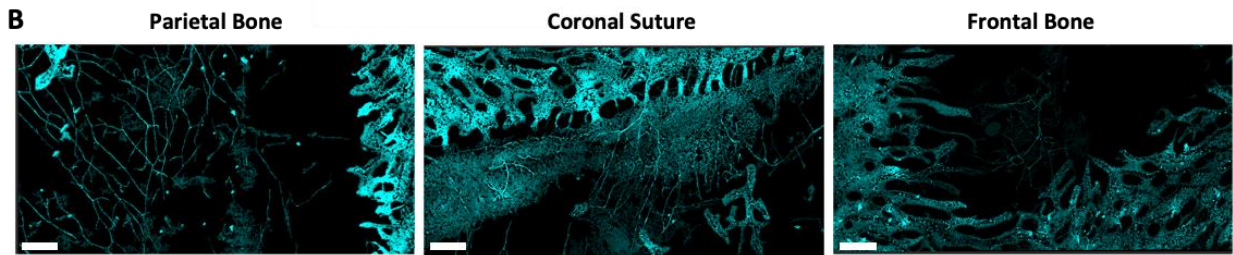
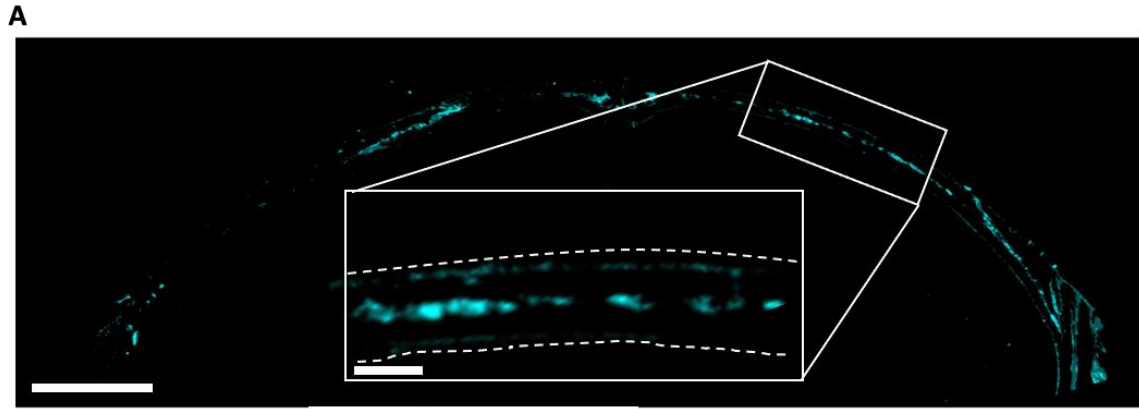
apathak2@jhmi.edu



633

Supplemental Figure 1: A method for quantitative analysis of 3D nerve structures acquired with QLSM. A) 4wk, 12wk, 40wk, and 80wk calvaria before and after tissue clearing with 2'2-thiodiethanol. B) Workflow of quantitative nerve analysis beginning with lightsheet imaging, followed image processing with Imaris®, ImageJ®, and Ilastik®. C) Comparison of segmentation of nerves using Imaris® and Ilastik® relative to the original fluorescent images acquired with QLSM. Scale bar is 250 μm . D) Imaris®-derived volume fraction for TUBB3+ nerves in the frontal bone region. E) Ilastik®-derived volume fraction for TUBB3+ nerves in the frontal bone region. Data are mean \pm SD. Statistics were performed with a two-way ANOVA with post-hoc Tukey HSD test. * $p < 0.5$ where designated.

634

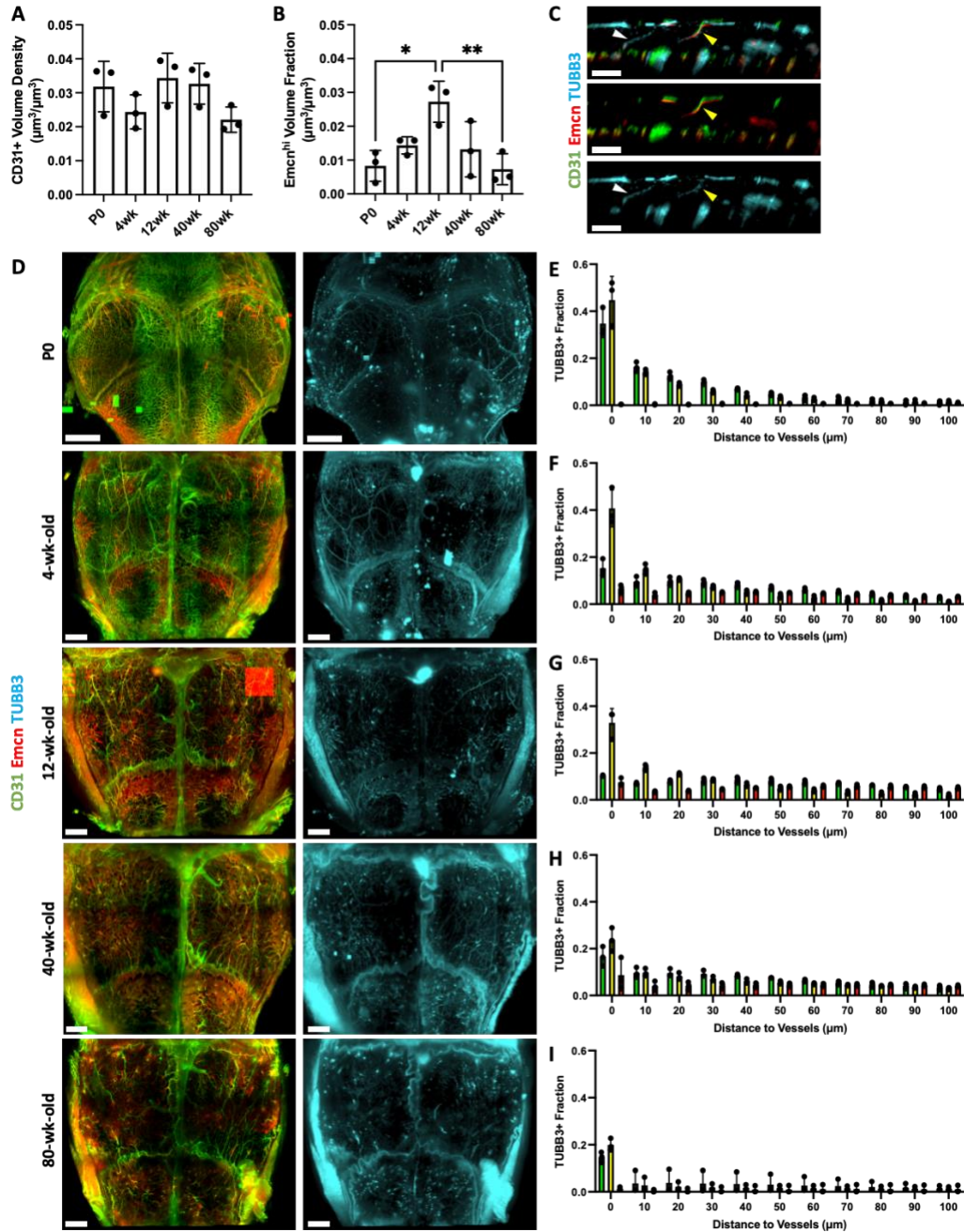


635

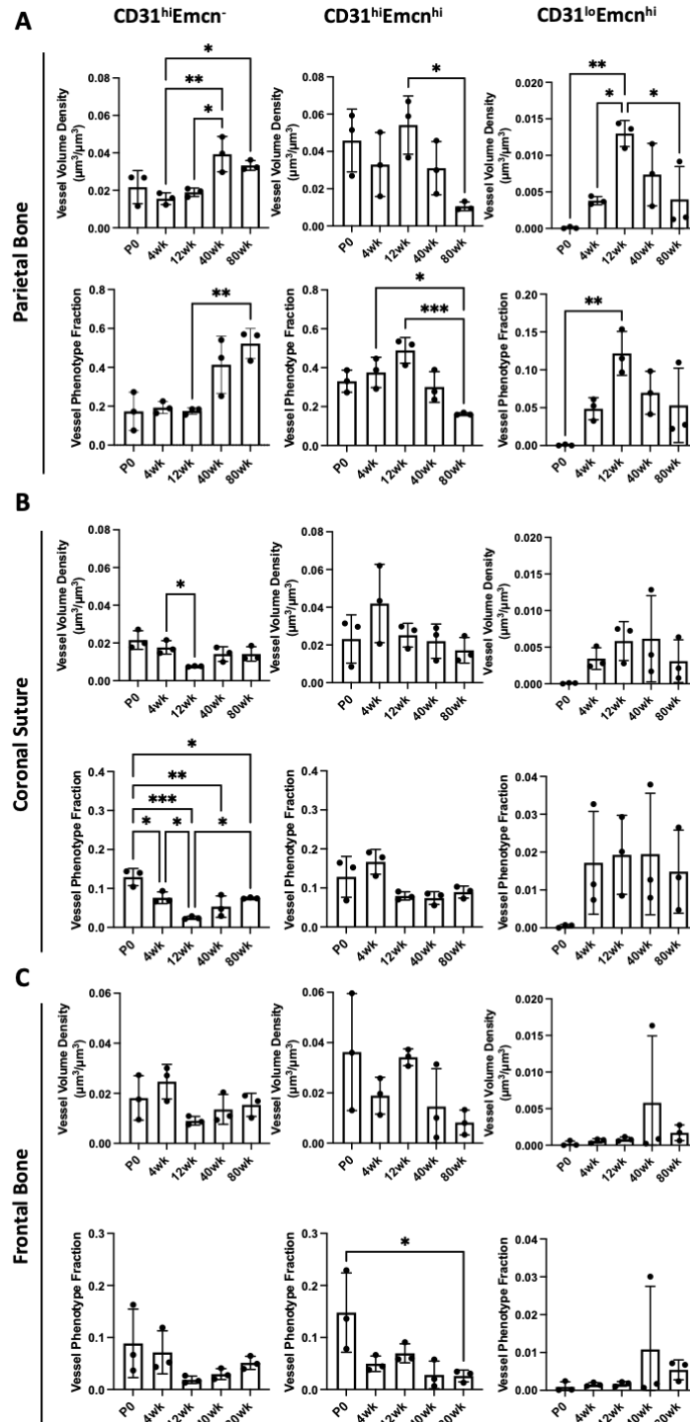
Supplemental Figure 2: Alternate methods for imaging calvarial nerves. A) 50 μm thick cross-section of TUBB3+ nerves from a coronal calvarium section. Scale bar is 1000 μm . Inset scale bar is 150 μm . B) MIP image acquired at 10x from confocal microscopy of the whole-mount calvarial tissue in the parietal bone, coronal suture, and frontal bone. Scale bar is 200 μm . C) MIP image acquired at 20x with confocal microscopy of whole-mount calvaria; tissue in the parietal bone. Scale bar is 50 μm .

636

637



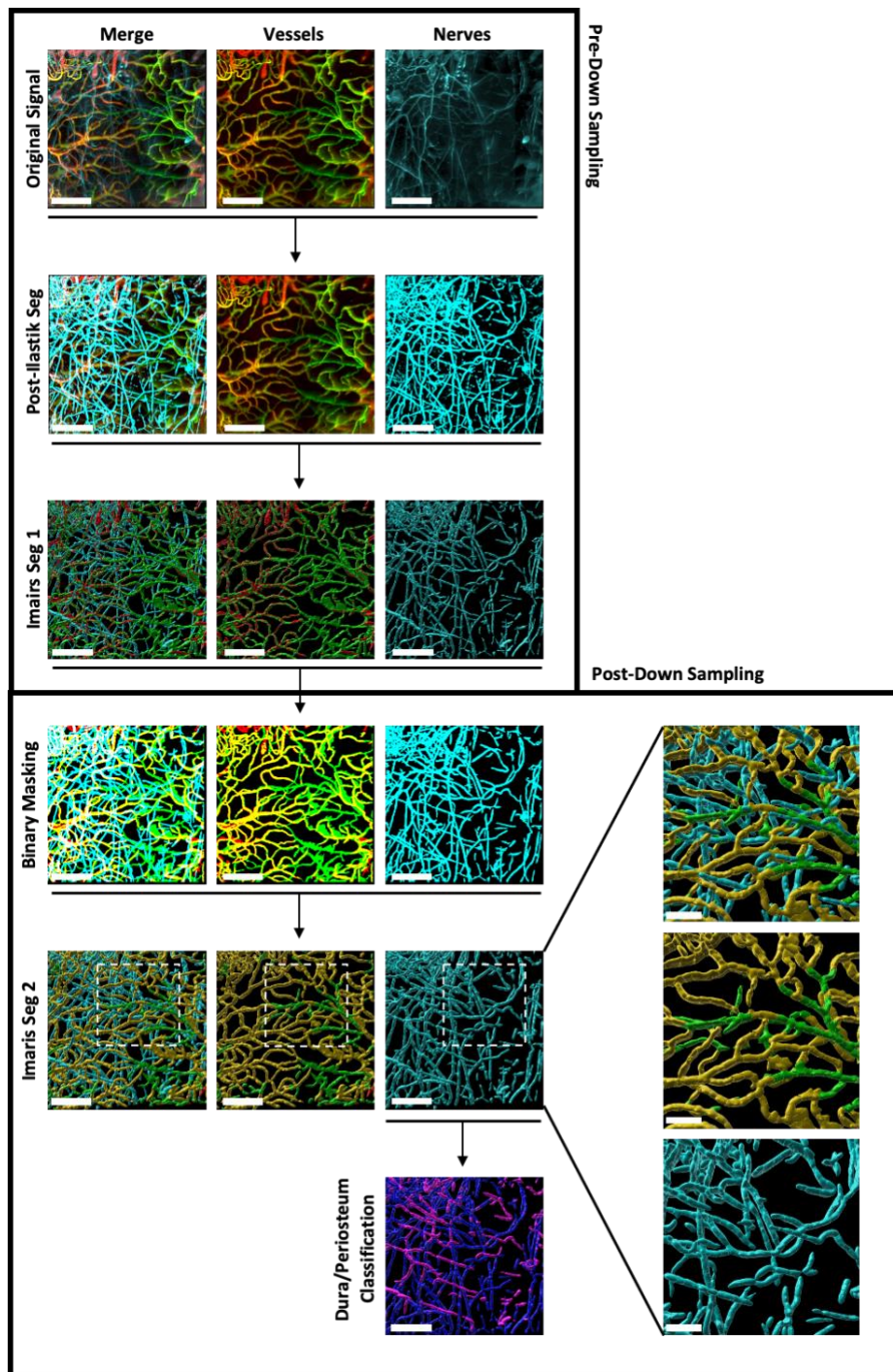
Supplemental Figure 3: Changes in TUBB3+ nerve interactions with vasculature during aging. A) Vessel volume calculations for CD31+ blood vessels for P0, 4wk, 12wk, 40wk, and 80wk calvaria. B) Vessel volume calculations for Emcn^{hi} blood vessels for P0, 4wk, 12wk, 40wk, and 80wk calvaria. C) 50 µm coronal cross-section of TUBB3+ nerves and CD31+ and Emcn+ blood vessels. White arrowheads represent nerves and yellow arrowheads indicate vessels in transcortical canals. Scale bar is 300 µm. D) Full calvaria MIP images for CD31+ and Emcn+ blood vessels and TUBB3+ nerves in P0, 4wk, 12wk, 40wk, and 80wk mice. Scale bar is 1000 µm. E-I) Spatial association histograms from TUBB3+ nerve association to CD31^{hi}Emcn⁻ (green), CD31^{hi}Emcn^{hi} (yellow), and CD31^{lo}Emcn^{hi} (red) blood vessels in E) P0, F) 4wk, G) 12wk, H) 40wk, and I) 80wk mice.



640
641

Supplemental Figure 4: Regional changes in vessel phenotype distributions over the mouse lifespan.

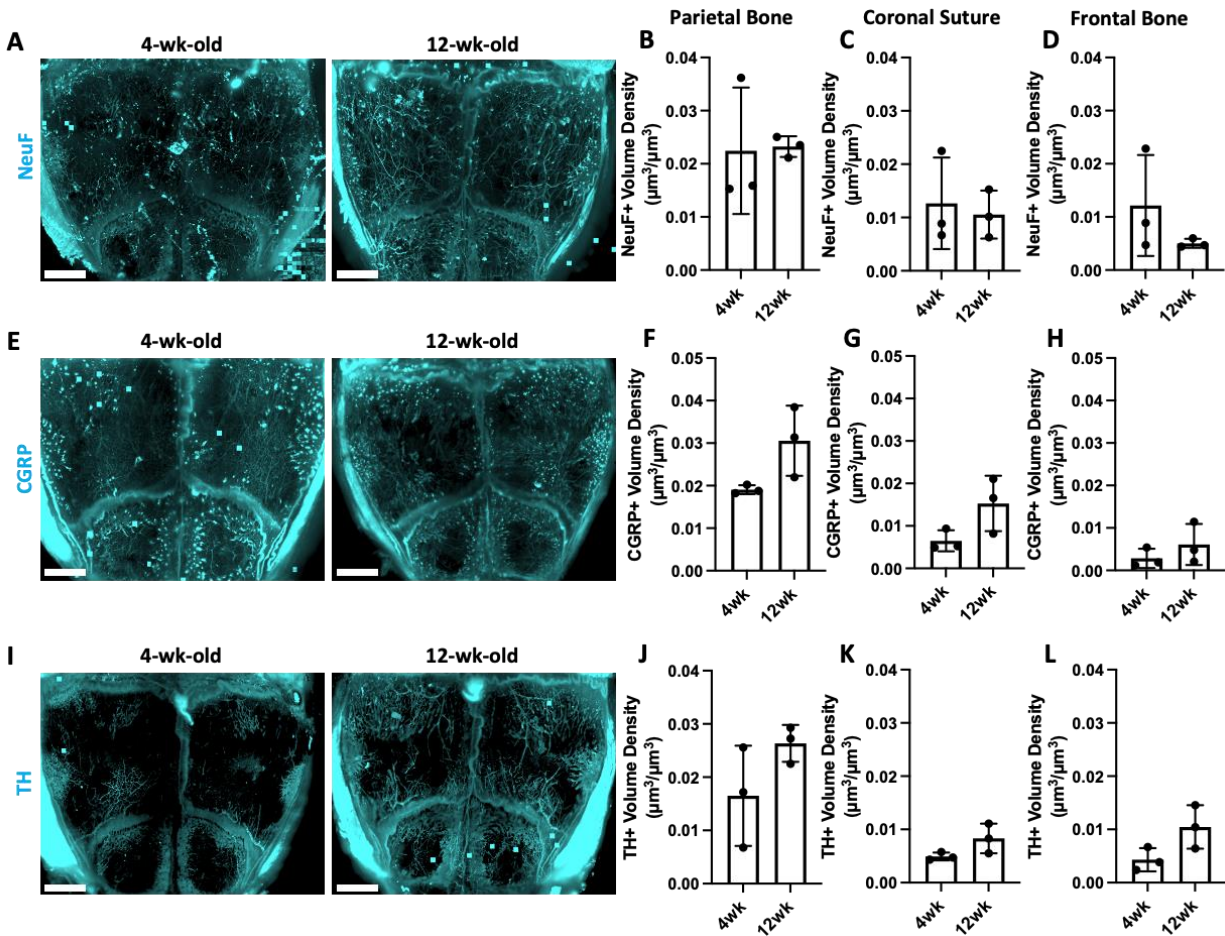
A) Vessel phenotype volume density and fraction for CD31^{hi}Emcn⁻, CD31^{hi}Emcn^{hi}, CD31^{lo}Emcn^{hi} blood vessels in the parietal bone for P0, 4wk, 12wk, 40wk, and 80wk calvaria. B) Vessel phenotype volume density and fraction for CD31^{hi}Emcn⁻, CD31^{hi}Emcn^{hi}, CD31^{lo}Emcn^{hi} blood vessels in the coronal suture region for P0, 4wk, 12wk, 40wk, and 80wk calvaria. C) Vessel phenotype volume density and fraction for CD31^{hi}Emcn⁻, CD31^{hi}Emcn^{hi}, CD31^{lo}Emcn^{hi} blood vessels in the frontal bone for P0, 4wk, 12wk, 40wk, and 80wk calvaria.



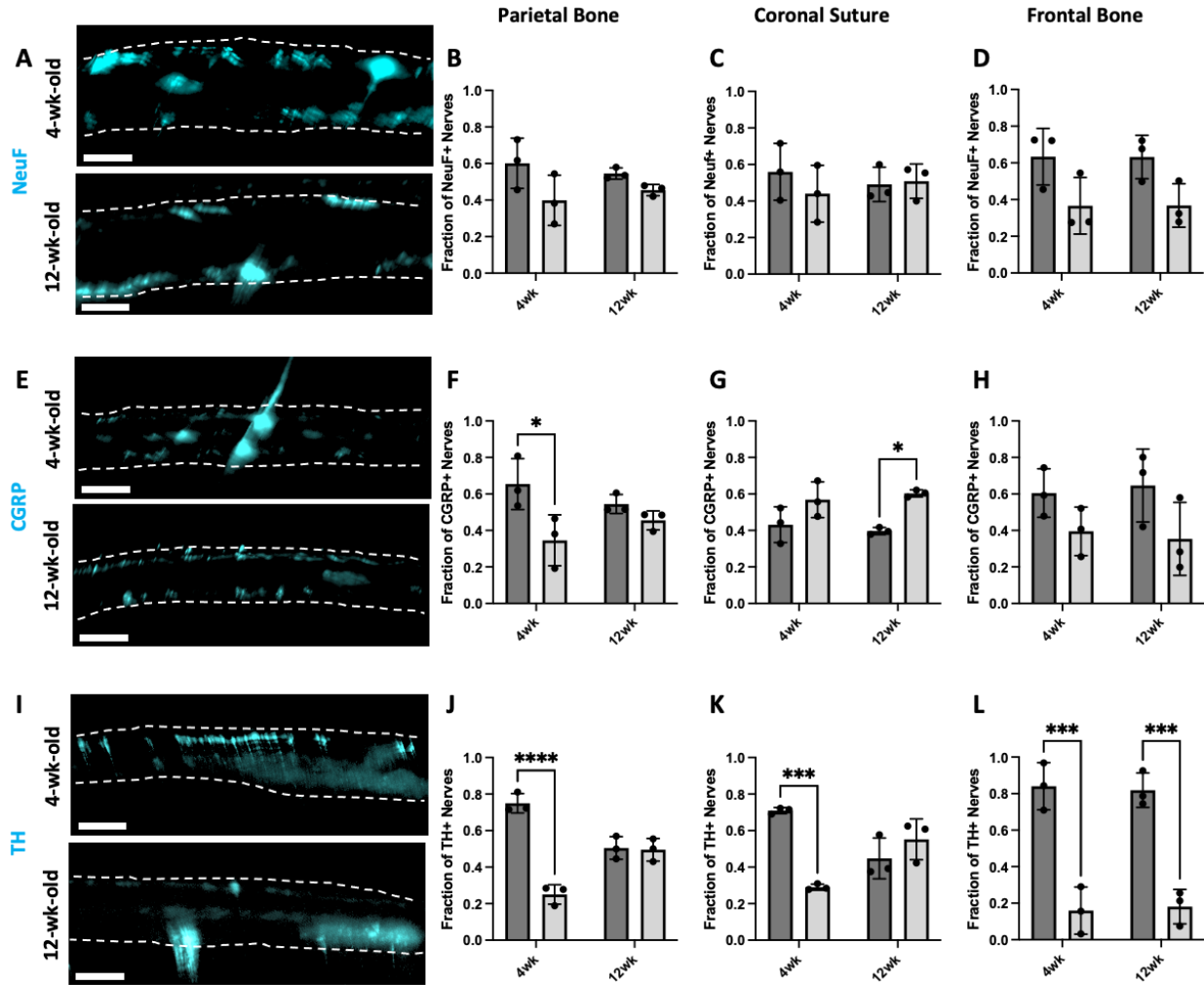
642

Supplemental Figure 5: Workflow for image quantification with Imaris®. Prior to spatial down-sampling and post-Ilastik® nerve segmentation, nerves and blood vessels undergo an initial segmentation with Imaris® to generate individual channel volume data. Following down-sampling, initial Imaris® segmentations are used to generate binary masks for each channel. Next, a secondary segmentation is conducted with Imaris® to generate vessel phenotype classifications, spatial association analysis, and dura/periosteum analysis. The secondary segmentation splits surfaces into 10 µm sections for subsequent analysis (zoomed region). Scale bars are 300 µm. Zoomed region scale bars are 150 µm.

643



Supplemental Figure 6: Regional changes in nerve subtype distributions during postnatal development. A) Full calvaria MIP images of 4wk and 12wk mice with NeuF+ nerves (blue). Scale bar is 1500 μm . B-D) Nerve volume fraction calculations for 4wk and 12wk NeuF+ nerves in the B) Parietal Bone region, C) Coronal Suture region, and D) Frontal Bone region. E) Full calvaria maximum intensity projections of 4wk and 12wk mice with CGRP+ nerves (blue). Scale bar is 300 μm . F-H) Nerve volume fraction calculations for 4wk and 12wk CGRP+ nerves in the F) Parietal Bone region, G) Coronal Suture region, and H) Frontal Bone region. I) Full calvaria maximum intensity projections of 4wk and 12wk mice with TH+ nerves (blue). Scale bar is 300 μm . J-L) Nerve volume fraction calculations for 4wk and 12wk TH+ nerves in the J) Parietal Bone region, K) Coronal Suture region, and L) Frontal Bone region. Data are mean \pm SD. Statistics were performed with a two-way ANOVA with post-hoc Tukey HSD test and a two-tailed t-test.

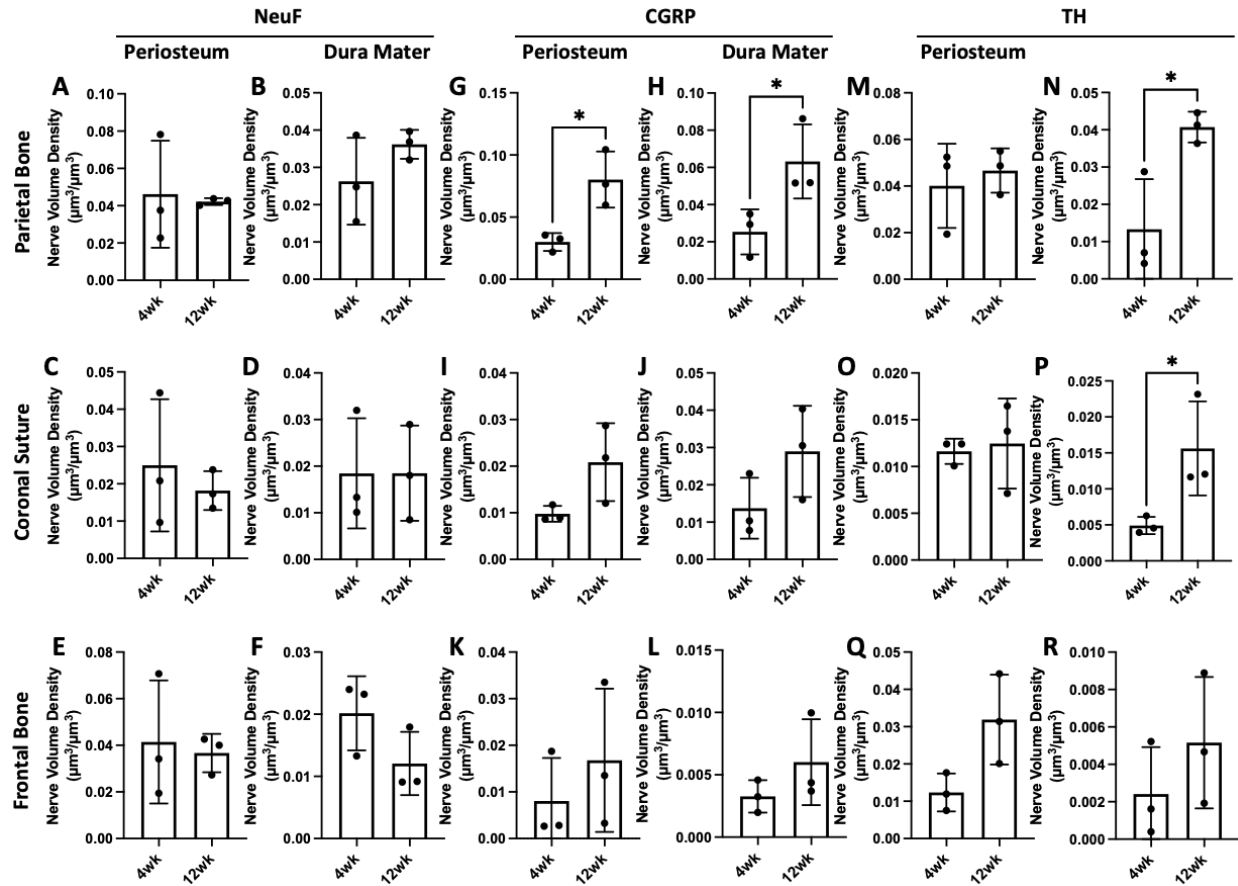


647

Supplemental Figure 7: Regional changes in nerve subtype dura and periosteum proportions during postnatal development. A) 50 μm coronal cross-sections of NeuF+ nerves in 4wk and 12wk mice. Scale bar is 300 μm . B-D) Dura and periosteum calculations for 4wk and 12wk NeuF+ nerves in the B) Parietal Bone region, C) Coronal Suture region, and D) Frontal Bone region. E) 50 μm coronal cross sections of CGRP+ nerves in 4wk and 12wk mice. Scale bar is 300 μm . F-H) Dura and periosteum calculations for 4wk and 12wk CGRP+ nerves in the F) Parietal Bone region, G) Coronal Suture region, and H) Frontal Bone region. I) 50 μm coronal cross sections of TH+ nerves in 4wk and 12wk mice. Scale bar is 300 μm . J-L) Dura and periosteum calculations for 4wk and 12wk TH+ nerves in the J) Parietal Bone region, K) Coronal Suture region, and L) Frontal Bone region. Data are mean \pm SD. Statistics were performed with a two-way ANOVA with post-hoc Tukey HSD test and a two-tailed t-test. * $p < 0.05$ and *** $p < 0.001$ where designated.

648

649



650

Supplemental Figure 8: Regional changes in nerve subtype dura and periosteum volume densities during postnatal development. A-F) Periosteal and dural nerve volume density calculations for NeuF+ nerves in 4wk and 12wk samples in A) Parietal Bone Region Periosteum, B) Parietal Bone Region Dura Mater, C) Coronal Suture Region Periosteum, D) Coronal Suture Region Dura Mater, E) Frontal Bone Region Periosteum, F) Frontal Bone Region Dura Mater. G-L) Periosteal and dural nerve volume density calculations for CGRP+ nerves in 4wk and 12wk samples in G) Parietal Bone Region Periosteum, H) Parietal Bone Region Dura Mater, I) Coronal Suture Region Periosteum, J) Coronal Suture Region Dura Mater, K) Frontal Bone Region Periosteum, L) Frontal Bone Region Dura Mater. M-R) Periosteal and dural nerve volume density calculations for TH+ nerves in 4wk and 12wk samples in M) Parietal Bone Region Periosteum, N) Parietal Bone Region Dura Mater, O) Coronal Suture Region Periosteum, P) Coronal Suture Region Dura Mater, Q) Frontal Bone Region Periosteum, R) Frontal Bone Region Dura Mater. Data are mean \pm SD. Statistics were performed with a two-way ANOVA with post-hoc Tukey HSD test. * $p < 0.5$ where designated.

651
652

653
654

Supplemental Table 1. List of all key reagents and resources used in this study.

Reagent or Resource	Source	Identifier
<i>Antibodies</i>		
Rabbit anti-mouse TUBB3 (1:200)	Abcam	ab18207
Rabbit anti-mouse NeuF (1:200)	Thermo Fisher Scientific	PA3-16721
Rabbit anti-mouse CGRP (1:200)	Sigma Aldrich	C8198
Rabbit anti-mouse TH (1:200)	Sigma Aldrich	AB152
Goat anti-mouse/rat CD31 (1:200)	R&D Systems	AF3628
Rat anti-mouse/rat Endomucin (1:50)	Santa Cruz Biotechnology	sc-65495
Donkey anti-goat AF800 plus, 0.67 mg/mL (1:100)	Thermo Fisher Scientific	A32930
Donkey anti-rabbit AF647 plus, 0.67 mg/mL (1:300)	Thermo Fisher Scientific	A32795
Donkey anti-rat biotin, 0.75 mg/mL (1:200)	Thermo Fisher Scientific	A18749
Streptavidin AF555 conjugate, 0.67 mg/mL (1:200)	Thermo Fisher Scientific	S32355
<i>Reagents</i>		
Heparin sodium salt from porcine mucosa	Sigma Aldrich	H3393-50KU
Paraformaldehyde, 16% aq. soln., methanol free	Alfa Aesar	433689M
Normal donkey serum	Sigma Aldrich	D9663-10ML
Trizma base	Sigma Aldrich	T6066-1KG
Trizma hydrochloride	Sigma Aldrich	T5941-1KG
Sodium chloride	Sigma Aldrich	S5886
Tween 20	Sigma Aldrich	P7949
Dimethylsulfoxide	Thermo Fisher Scientific	PI20688

655

- 657 1. Tomlinson, R. E. *et al.* NGF-TrkA Signaling by Sensory Nerves Coordinates the Vascularization and
658 Ossification of Developing Endochondral Bone. *Cell Rep.* **16**, 2723–2735 (2016).
- 659 2. Farr, J. N. & Khosla, S. Cellular senescence in bone. *Bone* **121**, 121–133 (2019).
- 660 3. Kim, H.-N. *et al.* DNA damage and senescence in osteoprogenitors expressing *Osx1* may cause
661 their decrease with age. *Aging Cell* **16**, 693–703 (2017).
- 662 4. Halloran, B. P. *et al.* Changes in bone structure and mass with advancing age in the male
663 C57BL/6J mouse. *J. Bone Miner. Res.* **17**, 1044–1050 (2002).
- 664 5. Pappert, M., Khosla, S. & Doolittle, M. Influences of aged bone marrow macrophages on skeletal
665 health and senescence. *Curr. Osteoporos. Rep.* **21**, 771–778 (2023).
- 666 6. Stucker, S., Chen, J., Watt, F. E. & Kusumbe, A. P. Bone angiogenesis and vascular niche
667 remodeling in stress, aging, and diseases. *Front. Cell Dev. Biol.* **8**, 602269 (2020).
- 668 7. Jimenez-Andrade, J. M. *et al.* A phenotypically restricted set of primary afferent nerve fibers
669 innervate the bone versus skin: therapeutic opportunity for treating skeletal pain. *Bone* **46**, 306–
670 313 (2010).
- 671 8. Mach, D. B. *et al.* Origins of skeletal pain: sensory and sympathetic innervation of the mouse
672 femur. *Neuroscience* **113**, 155–166 (2002).
- 673 9. Martin, C. D., Jimenez-Andrade, J. M., Ghilardi, J. R. & Mantyh, P. W. Organization of a unique
674 net-like meshwork of CGRP+ sensory fibers in the mouse periosteum: implications for the
675 generation and maintenance of bone fracture pain. *Neurosci. Lett.* **427**, 148–152 (2007).
- 676 10. Steverink, J. G. *et al.* Sensory innervation of human bone: an immunohistochemical study to
677 further understand bone pain. *J. Pain* **22**, 1385–1395 (2021).
- 678 11. Martin, P. & Lewis, J. Origins of the neurovascular bundle: interactions between developing
679 nerves and blood vessels in embryonic chick skin. *Int. J. Dev. Biol.* **33**, 379–387 (1989).
- 680 12. Mukouyama, Y., Shin, D., Britsch, S., Taniguchi, M. & Anderson, D. J. Sensory nerves determine
681 the pattern of arterial differentiation and blood vessel branching in the skin. *Cell* **109**, 693–705
682 (2002).
- 683 13. Li, W. *et al.* Peripheral nerve-derived CXCL12 and VEGF-A regulate the patterning of arterial
684 vessel branching in developing limb skin. *Dev. Cell* **24**, 359–371 (2013).
- 685 14. Bjurholm, A., Kreicbergs, A., Terenius, L., Goldstein, M. & Schultzberg, M. Neuropeptide Y-,
686 tyrosine hydroxylase- and vasoactive intestinal polypeptide-immunoreactive nerves in bone and
687 surrounding tissues. *J. Auton. Nerv. Syst.* **25**, 119–125 (1988).
- 688 15. Bjurholm, A., Kreicbergs, A., Brodin, E. & Schultzberg, M. Substance P- and CGRP-immunoreactive
689 nerves in bone. *Peptides* **9**, 165–171 (1988).
- 690 16. Hill, E. L. & Elde, R. Distribution of CGRP-, VIP-, D beta H-, SP-, and NPY-immunoreactive nerves in
691 the periosteum of the rat. *Cell Tissue Res.* **264**, 469–480 (1991).
- 692 17. Asmus, S. E., Parsons, S. & Landis, S. C. Developmental changes in the transmitter properties of
693 sympathetic neurons that innervate the periosteum. *J. Neurosci.* **20**, 1495–1504 (2000).
- 694 18. Coutu, D. L., Kokkaliaris, K. D., Kunz, L. & Schroeder, T. Three-dimensional map of
695 nonhematopoietic bone and bone-marrow cells and molecules. *Nat. Biotechnol.* **35**, 1202–1210
696 (2017).
- 697 19. Sayilekshmy, M. *et al.* Innervation is higher above Bone Remodeling Surfaces and in Cortical
698 Pores in Human Bone: Lessons from patients with primary hyperparathyroidism. *Sci. Rep.* **9**, 5361
699 (2019).
- 700 20. Li, J., Ahmad, T., Spetea, M., Ahmed, M. & Kreicbergs, A. Bone reinnervation after fracture: a
701 study in the rat. *J. Bone Miner. Res.* **16**, 1505–1510 (2001).

- 702 21. Alberius, P. & Skagerberg, G. Adrenergic innervation of the calvarium of the neonatal rat. Its
703 relationship to the sagittal suture and developing parietal bones. *Anat. Embryol.* **182**, 493–498
704 (1990).
- 705 22. Kusumbe, A. P., Ramasamy, S. K. & Adams, R. H. Coupling of angiogenesis and osteogenesis by a
706 specific vessel subtype in bone. *Nature* **507**, 323–328 (2014).
- 707 23. Ramasamy, S. K., Kusumbe, A. P., Wang, L. & Adams, R. H. Endothelial Notch activity promotes
708 angiogenesis and osteogenesis in bone. *Nature* **507**, 376–380 (2014).
- 709 24. Tower, R. J. *et al.* Spatial transcriptomics reveals a role for sensory nerves in preserving cranial
710 suture patency through modulation of BMP/TGF- β signaling. *Proc Natl Acad Sci USA* **118**, (2021).
- 711 25. Wang, Y. *et al.* Abnormalities in cartilage and bone development in the Apert syndrome
712 FGFR2(+/*S252W*) mouse. *Development* **132**, 3537–3548 (2005).
- 713 26. Aldridge, K. *et al.* Brain phenotypes in two FGFR2 mouse models for Apert syndrome. *Dev. Dyn.*
714 **239**, 987–997 (2010).
- 715 27. Motch Perrine, S. M. *et al.* Integration of brain and skull in prenatal mouse models of Apert and
716 Crouzon syndromes. *Front. Hum. Neurosci.* **11**, 369 (2017).
- 717 28. Holmes, G. *et al.* Midface and upper airway dysgenesis in FGFR2-related craniosynostosis involves
718 multiple tissue-specific and cell cycle effects. *Development* **145**, (2018).
- 719 29. Motch Perrine, S. M. *et al.* Mandibular dysmorphology due to abnormal embryonic osteogenesis
720 in FGFR2-related craniosynostosis mice. *Dis. Model. Mech.* **12**, (2019).
- 721 30. Motch Perrine, S. M. *et al.* A dysmorphic mouse model reveals developmental interactions of
722 chondrocranium and dermatocranium. *eLife* **11**, (2022).
- 723 31. Martínez-Abadías, N. *et al.* Beyond the closed suture in apert syndrome mouse models: evidence
724 of primary effects of FGFR2 signaling on facial shape at birth. *Dev. Dyn.* **239**, 3058–3071 (2010).
- 725 32. Lorenz, M. R., Brazill, J. M., Beeve, A. T., Shen, I. & Scheller, E. L. A neuroskeletal atlas: spatial
726 mapping and contextualization of axon subtypes innervating the long bones of C3H and B6 mice.
727 *J. Bone Miner. Res.* **36**, 1012–1025 (2021).
- 728 33. Kosaras, B., Jakubowski, M., Kainz, V. & Burstein, R. Sensory innervation of the calvarial bones of
729 the mouse. *J. Comp. Neurol.* **515**, 331–348 (2009).
- 730 34. Rindone, A. N. *et al.* Quantitative 3D imaging of the cranial microvascular environment at single-
731 cell resolution. *Nat. Commun.* **12**, 6219 (2021).
- 732 35. Berg, S. *et al.* ilastik: interactive machine learning for (bio)image analysis. *Nat. Methods* **16**,
733 1226–1232 (2019).
- 734 36. Schneider, C. A., Rasband, W. S. & Eliceiri, K. W. NIH Image to ImageJ: 25 years of image analysis.
735 *Nat. Methods* **9**, 671–675 (2012).
- 736 37. Little, G. J. & Heath, J. W. Morphometric analysis of axons myelinated during adult life in the
737 mouse superior cervical ganglion. *J. Anat.* **184 (Pt 2)**, 387–398 (1994).
- 738 38. Topley, M. *et al.* Evaluation of motor and sensory neuron populations in a mouse median nerve
739 injury model. *J. Neurosci. Methods* **396**, 109937 (2023).
- 740 39. Dutta, S. & Sengupta, P. Men and mice: Relating their ages. *Life Sci.* **152**, 244–248 (2016).
- 741 40. Staaf, S., Franck, M. C. M., Marmigère, F., Mattsson, J. P. & Ernfors, P. Dynamic expression of the
742 TRPM subgroup of ion channels in developing mouse sensory neurons. *Gene Expr. Patterns* **10**,
743 65–74 (2010).
- 744 41. He, H. *et al.* CGRP may regulate bone metabolism through stimulating osteoblast differentiation
745 and inhibiting osteoclast formation. *Mol. Med. Report.* **13**, 3977–3984 (2016).
- 746 42. Wee, N. K. Y. *et al.* Inhibition of CGRP signaling impairs fracture healing in mice. *J. Orthop. Res.*
747 **41**, 1228–1239 (2023).
- 748 43. McLean, J. H. & Shipley, M. T. Postmitotic, postmigrational expression of tyrosine hydroxylase in
749 olfactory bulb dopaminergic neurons. *J. Neurosci.* **8**, 3658–3669 (1988).

- 750 44. Willing, J., Cortes, L. R., Brodsky, J. M., Kim, T. & Juraska, J. M. Innervation of the medial
751 prefrontal cortex by tyrosine hydroxylase immunoreactive fibers during adolescence in male and
752 female rats. *Dev. Psychobiol.* **59**, 583–589 (2017).
- 753 45. Kedzierski, W. & Porter, J. C. Quantitative study of tyrosine hydroxylase mRNA in
754 catecholaminergic neurons and adrenals during development and aging. *Brain Res. Mol. Brain*
755 *Res.* **7**, 45–51 (1990).
- 756 46. Sharma, N. *et al.* The emergence of transcriptional identity in somatosensory neurons. *Nature*
757 **577**, 392–398 (2020).
- 758 47. Chartier, S. R., Mitchell, S. A. T., Majuta, L. A. & Mantyh, P. W. The changing sensory and
759 sympathetic innervation of the young, adult and aging mouse femur. *Neuroscience* **387**, 178–190
760 (2018).
- 761 48. Tomlinson, R. E. *et al.* NGF-TrkA signaling in sensory nerves is required for skeletal adaptation to
762 mechanical loads in mice. *Proc Natl Acad Sci USA* **114**, E3632–E3641 (2017).
- 763 49. Wu, Q., Yang, B., Cao, C., Guang, M. & Gong, P. Age-dependent impact of inferior alveolar nerve
764 transection on mandibular bone metabolism and the underlying mechanisms. *J. Mol. Histol.* **47**,
765 579–586 (2016).
- 766 50. Zhao, J. & Levy, D. The sensory innervation of the calvarial periosteum is nociceptive and
767 contributes to headache-like behavior. *Pain* **155**, 1392–1400 (2014).
- 768 51. Meyers, C. A. *et al.* A neurotrophic mechanism directs sensory nerve transit in cranial bone. *Cell*
769 *Rep.* **31**, 107696 (2020).
- 770 52. Fujita, S. *et al.* Quantitative analysis of sympathetic and nociceptive innervation across bone
771 marrow regions in mice. *Exp. Hematol.* **112–113**, 44–59.e6 (2022).
- 772 53. Cantarella, G. *et al.* Nerve growth factor-endothelial cell interaction leads to angiogenesis in vitro
773 and in vivo. *FASEB J.* **16**, 1307–1309 (2002).
- 774 54. Nakamura, K., Tan, F., Li, Z. & Thiele, C. J. NGF activation of TrkA induces vascular endothelial
775 growth factor expression via induction of hypoxia-inducible factor-1 α . *Mol. Cell. Neurosci.* **46**,
776 498–506 (2011).
- 777 55. Li, Z. *et al.* Fracture repair requires TrkA signaling by skeletal sensory nerves. *J. Clin. Invest.* **129**,
778 5137–5150 (2019).
- 779 56. Adams, R. *et al.* Adult skull bone marrow is an expanding and resilient hematopoietic reservoir.
780 *Res. Sq.* (2023) doi:10.21203/rs.3.rs-3426773/v1.
- 781 57. Tholpady, S. S. *et al.* Aberrant bony vasculature associated with activating fibroblast growth
782 factor receptor mutations accompanying Crouzon syndrome. *J. Craniofac. Surg.* **15**, 431–5;
783 discussion 436 (2004).
- 784 58. Tischfield, M. A. *et al.* Cerebral Vein Malformations Result from Loss of Twist1 Expression and
785 BMP Signaling from Skull Progenitor Cells and Dura. *Dev. Cell* **42**, 445–461.e5 (2017).
- 786 59. Breik, O. *et al.* Central nervous system and cervical spine abnormalities in Apert syndrome. *Childs*
787 *Nerv Syst* **32**, 833–838 (2016).
- 788 60. Yeh, E. *et al.* Novel molecular pathways elicited by mutant FGFR2 may account for brain
789 abnormalities in Apert syndrome. *PLoS ONE* **8**, e60439 (2013).
- 790 61. Wang, Y. *et al.* Activation of p38 MAPK pathway in the skull abnormalities of Apert syndrome
791 Fgfr2(+P253R) mice. *BMC Dev. Biol.* **10**, 22 (2010).